JOURNAL OF GEOPHYSICAL RESEARCH: PLANETS, VOL. 118, 1–9, doi:10.1002/jgre.20125, 2013

ARTEMIS observations of lunar pickup ions: Mass constraints on ion species

X.-Z. Zhou,[1,2] V. Angelopoulos,[1,2] A. R. Poppe,[3] and J. S. Halekas[3]

Received 27 May 2013; revised 29 July 2013; accepted 13 August 2013.

[1] Observations of heavy ions of lunar origin give important information regarding lunar exospheric processes, especially with respect to exospheric particle abundance and composition. Electrostatic analyzers without a time-of-flight section provide highly sensitive, absolute density detection but without mass discrimination. Here we place constraints on lunar ion species through inference of the average ion mass using such instruments. The technique is based on the plasma quasi-neutrality requirement, an independent electron density measurement, and the fact that electrostatic analyzers underestimate the ion density by the square root of the ion mass. Applied to a case of such observations by ARTEMIS in the terrestrial lobe reported by Poppe et al. (2012), our technique suggests an average mass of 28 amu for lunar pickup ions. This result, consistent with the lower limit of 24 amu derived in the Poppe et al. model, suggests that the observed ions were most likely Al^+ and Si^+. The technique is also refined and applied to a more complicated event with a series of heavy ion surges in the plasma sheet, to show the spatial and/or temporal dependence of the observed lunar ion species. The technique is particularly timely given the planned conjunctions and coordinated lunar studies by NASA's Acceleration, Reconnection, Turbulence and Electrodynamics of the Moon's Interaction with the Sun (ARTEMIS) and Lunar Atmosphere and Dust Environment Explorer missions.

Citation: Zhou, X.-Z., V. Angelopoulos, A. R. Poppe, and J. S. Halekas (2013), ARTEMIS observations of lunar pickup ions: Mass constraints on ion species, *J. Geophys. Res. Planets*, *118*, doi:10.1002/jgre.20125.

1. Introduction

[2] The lunar exosphere, a tenuous layer surrounding the Moon, contains a variety of neutral species [*Stern*, 1999]. Photoionization of these neutrals generates heavy ions to be picked up by the ambient plasma, which are easier to detect and can thus be used to infer the exospheric neutral composition. These pickup ions have been observed by the AMPTE [*Hilchenbach et al.*, 1993], WIND [*Mall et al.*, 1998], KAGUYA [*Tanaka et al.*, 2009; *Yokota et al.*, 2009], and Chang'e [*Wang et al.*, 2011] spacecraft, and species including H_2^+, He^+, C^+, O^+, OH^+, Na^+/Mg^+, Al^+, Si^+, K^+, and Ar^+/Ca^+ have been identified.

[3] More recently, observations from the Acceleration, Reconnection, Turbulence and Electrodynamics of the Moon's Interaction with the Sun (ARTEMIS) spacecraft have also shown the presence of lunar pickup ions [*Poppe et al.*, 2012; *Halekas et al.*, 2012, 2013]. With a geometric factor higher than typical time-of-flight spectrometers, the well-calibrated plasma instrument (the electrostatic analyzer, ESA [*McFadden et al.*, 2008a]) on board ARTEMIS can detect pickup ions sensitively (even at low flux levels) and compute their density precisely. However, the ESA's lack of direct mass-resolving capabilities makes identification of ion species more difficult; other characteristics of these heavy ions have to be used. In a case study of two events in the terrestrial lobes above the dayside lunar surface, *Poppe et al.* [2012] utilized the relationship between ion mass and the maximum energy those ions can gain during their gyration (in the presence of convection electric field) to obtain the average ion masses of over 29 and 24 amu, respectively. The most likely constituents, therefore, include Na^+, Al^+, Si^+, K^+, and Ar^+.

[4] The *Poppe et al.* [2012] approach, however, provides only a lower limit of the possible ion mass, as the heavy ions observed were not necessarily at their maximum energy. The approach also relies on magnetospheric convection models, rather than using direct electric field measurements given the large error of the measured electric field in the lobe region with very low plasma density. Therefore, a model-independent technique is required to verify their results and to place more accurate constraints on lunar ion species.

[1]Department of Earth and Space Sciences, University of California, Los Angeles, California, USA.
[2]Institute of Geophysics and Planetary Physics, University of California, Los Angeles, California, USA.
[3]Space Science Laboratory, University of California, Berkeley, California, USA.

Corresponding author: X.-Z. Zhou, Department of Earth and Space Sciences, University of California, 595 Charles Young Drive East, Los Angeles, CA 90095, USA. (xzhou@igpp.ucla.edu)

2169-9097/13/10.1002/jgre.20125

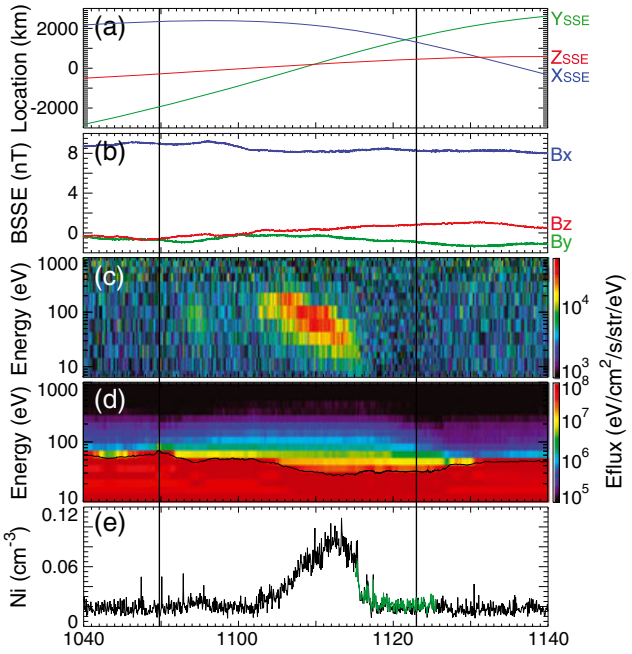

Figure 1. Overview of ARTEMIS P2 observations on 11 November 2011. (a) ARTEMIS P2 location in the SSE (selenocentric solar ecliptic) coordinates; (b) magnetic field components in SSE; (c) ion energy spectra; (d) electron energy spectra, with the black line representing the spacecraft potential; and (e) ion density, the zero-order moment of the measured ion distribution functions, integrated under the assumption that these ions are protons. The overlapping green line is the ion density integrated from high-resolution particle-burst data. The vertical lines demarcate the time interval when P2 was magnetically connected with the underlying lunar surface.

[5] Another approach to infer the average ion mass, first proposed by *Nosé et al.* [2011] when analyzing the CRRES data to indicate the O^+ existence near the plasmapause, is based on the plasma quasi-neutrality assumption. The approach requires measurements of the plasma mass density (ρ, estimated from the frequency of the fundamental standing Alfvén waves) and the electron density (n_e), and suggests that their quotient (ρ/n_e) be the local average ion mass. However, the *Nosé et al.* [2011] approach cannot be applied to the lunar vicinity as its applicability is largely restricted to the inner magnetosphere where standing Alfvén waves are present.

[6] In this paper, we propose a new technique to determine the average mass of heavy ions observed by electrostatic analyzers. The technique is also based on the plasma quasi-neutrality requirement, together with the fact that electrostatic analyzers underestimate the ion density by the square root of the ion mass. In section 2, we briefly introduce the ARTEMIS instruments we use and then discuss the basis of our new technique. In section 3, we apply the technique to one of the *Poppe et al.* [2012] events in the terrestrial lobe and compare our results with theirs. In section 4, the technique is further refined to be applied to a more complicated event in the plasma sheet with multiple surges of lunar heavy ions, before we summarize the study in section 5.

2. Instrumentation and Methodology

[7] The ARTEMIS mission [*Angelopoulos*, 2011], an extension of Time History of Events and Macroscale Interactions during Substorms (THEMIS) mission [*Angelopoulos*, 2008], redeployed two of the five identically instrumented THEMIS spacecraft (P1 and P2) to lunar orbits. This study uses data from the following ARTEMIS instruments: (1) the fluxgate magnetometer (FGM) [*Auster et al.*, 2008], which provides magnetic field measurements; (2) the electric field instrument (EFI) [*Bonnell et al.*, 2008], which measures electric field and spacecraft potential; and (3) the electrostatic analyzer (ESA) [*McFadden et al.*, 2008a], a highly sensitive plasma instrument that measures 3-D ion and electron distributions from a few eV to 25 keV.

[8] The collected ESA data are formatted into several different data products [*McFadden et al.*, 2008a]. These products include high-resolution "burst" packets which are available only within a few selected intervals (each lasting several minutes, referred to as particle-burst intervals) per orbit, and more consecutive "full" and "reduced" packets with reduced time, solid angle, and/or energy resolutions. In this paper, the "reduced" and, when available, the "burst" packets are used.

[9] As mentioned previously, electrostatic analyzers do not resolve mass, and it is usually assumed that all observed ions are protons. Given a singly charged ion mass of M amu, this assumption overestimates the ion speed by a factor of $\sqrt{M}$ as the instruments were designed to measure the energy per charge correctly. Since the particle flux produced by this ion does not depend on mass, the ion's contribution to the plasma density would be underestimated by the same factor of $\sqrt{M}$ [*McFadden et al.*, 2008b]. Plasma charge quasi-neutrality, however, requires that ion and electron densities be equal. Therefore, the best match between the mass-corrected ion density (or its variation from the background density in the presence of heavy ions) and the measured electron density (or its corresponding variation) should provide the average mass of the heavy ions.

[10] Although simple in principle, this approach requires accurate computation of both ion densities (before mass corrections) and electron densities. Such computations were made possible by extensive ground and in-flight calibrations of the plasma sensors [*McFadden et al.*, 2008a], although several other error sources summarized in *McFadden et al.* [2008b] must be also considered. The most significant error, especially for events in the tenuous lobe and/or outer plasma sheet regions, arises from the large spacecraft potential that repels ambient cold ions and at the same time attracts spacecraft-generated photoelectrons. Therefore, spacecraft potential measurements (provided by EFI) must be used. Detailed methods of eliminating these errors will be discussed in the next section when we apply the technique to the *Poppe et al.* [2012] event on 11 November 2011.

3. The 11 November 2011 Event

[11] Figure 1 provides an overview of ARTEMIS P2 observations during its lunar flyby on 11 November 2011 [*Poppe et al.*, 2012, 2013] when the Moon was in the terrestrial magnetotail at GSE $[-62.5, -7.5, 2.0]\,R_E$. The P2 location with respect to the Moon is shown in Figure 1a. The magnetic field (in Figure 1b) has a predominant B_x

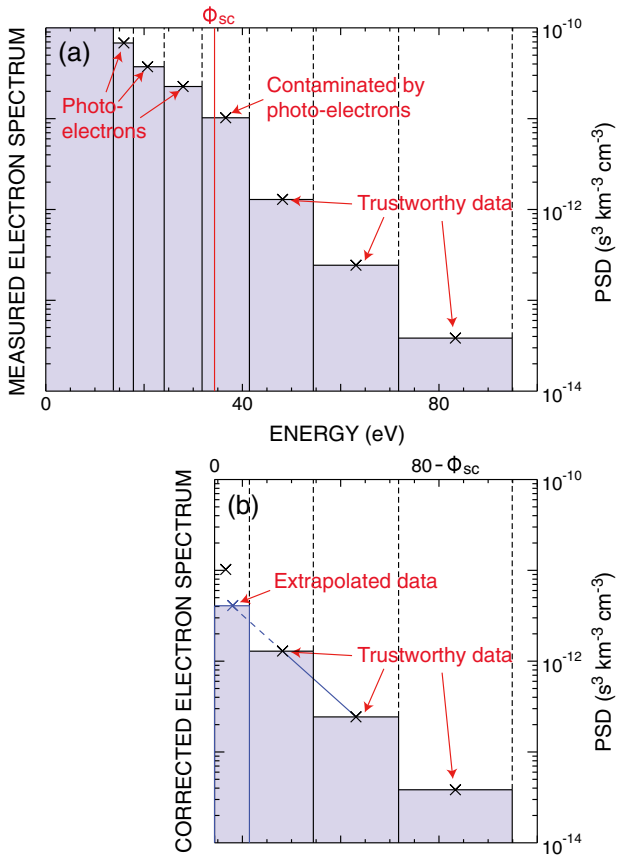

Figure 2. ARTEMIS P2 observations of the electron phase space densities at 11:07:33 UT as functions of energy. (a) The original data, with the vertical red line representing the spacecraft potential and the dashed lines separating different energy channels; (b) the corrected spectrum. The electron density and temperature are obtained by integrations over the shaded areas.

component, suggesting that P2 was in the north lobe. During the interval bounded by the two vertical lines, B_x dominated field lines connected the spacecraft (near periapsis, altitude from 300 to 1200 km) with the underlying dayside lunar surface.

[12] Figures 1c and 1d show the omnidirectional energy spectra of ions and electrons, respectively. From 1053 to 1056 UT, and more significantly from 1102 to 1117 UT, ion energy fluxes were enhanced at energies below 200 eV. These cold ions, mostly moving away from the Moon, were generated by photoionization of lunar neutrals before being accelerated upward by the lunar photoelectric field and at the same time picked up by magnetotail convection [*Poppe et al.*, 2012, 2013]. The detection of upward moving lunar ions at such low altitude, according to *Poppe et al.* [2013], most likely appears in the region magnetically connected with the Moon (between the two vertical lines in Figure 1), which agrees with our observations. The electron spectrum, on the other hand, shows the existence of low-energy spacecraft-generated photoelectrons with very high fluxes. These photoelectrons, to be eliminated later in the density computations, are roughly separated from ambient electrons by the EFI-measured spacecraft potential (black line). Note that the ambient electron fluxes were enhanced from 1102 to 1126 UT, approximately when lunar ions were present. This increased density is attributable to quasi-neutrality.

3.1. Ion Density Measurements

[13] We next integrate the measured ion distribution functions to obtain ion density N_i under the assumption that all these ions are protons. Before integration, the distribution functions were processed to remove the one-count level at the lowest energy channels (lower than one half of the spacecraft potential Φ_{sc}), a procedure implemented to reduce the background ion counts and ensure the statistical consistency with densities derived from spacecraft potential (J. McFadden, private communication, 2013). Also, the measured energy of each ion was adjusted (by adding Φ_{sc}) before integration, to take into account the ion deceleration effect due to the positive spacecraft charging. This deceleration effect can also hinder ESA's ability to record very cold ions (energies lower than Φ_{sc}) as they would be repelled from P2. Fortunately for this case, the lunar ions were unlikely cold enough to be missed as they mostly appeared at higher energies, except at 1114 UT when their energies decreased to the lowest energy channel (see Figure 1c, the ion fluxes at 6–8 eV became slightly above noise level). In other words, the integrated ion density should be accurate with few ions unrecorded before 1114 UT. After that, the ion density could be underestimated if these ions continue to decrease in energy and become unmeasurable.

[14] Figure 1e shows the resultant ion density (still under the proton assumption), and the overlapping green line shows the ion density integrated from the high-resolution "burst" data (the higher energy resolution during the 1115–1125 UT particle-burst interval can be seen in the ion spectrum of Figure 1c). The density profile suggests two ion sources: the presumably proton-dominated lobe population with a rather stable density (N_p) and the pickup heavy ions with density N_h peaking at $\sim$ 1112 UT.

[15] We keep in mind that this integrated ion density ($N_i(t)$ or $N_p + N_h(t)$) is not real. The mass-corrected ion density N_{ic} should be $N_p + \sqrt{M}\cdot[N_i(t) - N_p]$, where M and N_p are the two parameters to be determined later on by the required equality between N_{ic} and the electron density N_e.

3.2. Electron Density Measurements

[16] Our next step is to compute the electron density N_e, which is made more difficult by photoelectron contamination. Figure 2a is a sample electron spectrum (measured at 11:07:33 UT). Photoelectrons, characterized by significantly higher fluxes than those of the ambient population, mostly appear at energies below the spacecraft potential (represented by the vertical solid line). The separation at Φ_{sc} is not completely clean [*McFadden et al.*, 2008b], however. Measurements at energy channels just above Φ_{sc} could be heavily contaminated (see Figure 2a, the electron flux at the first energy channel above Φ_{sc} is much higher than those at higher energies and is closer to the photoelectron flux level). Therefore, these photoelectrons must be removed from the ambient plasma.

[17] The most straightforward way is to avoid measurements from suspicious energy channels just above Φ_{sc}. We only preserve those channels with lower boundaries at least

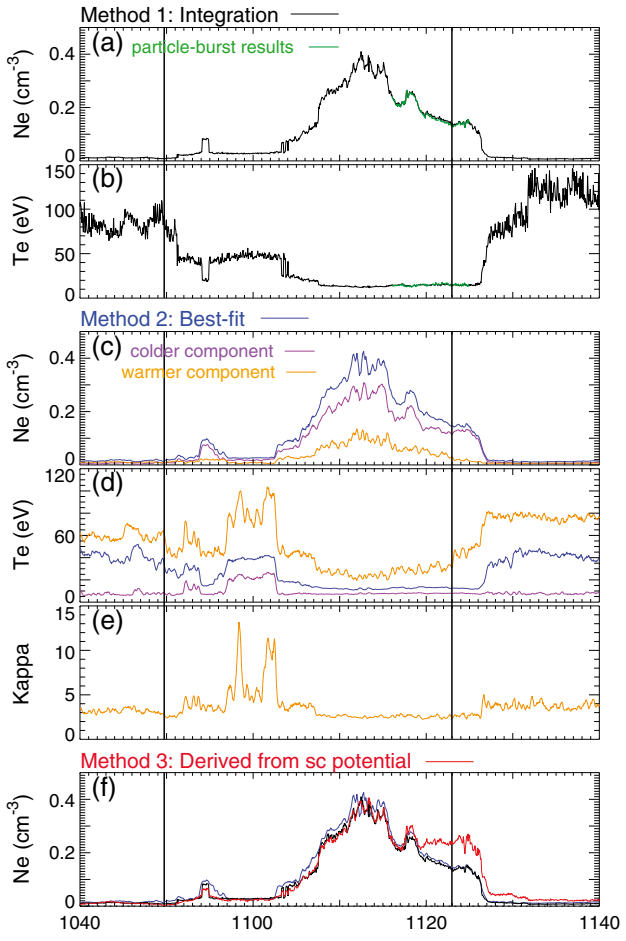

Figure 3. Electron density and associated quantities estimated from three different methods. (a) Electron density and (b) temperature computed by integrating the corrected spectra; (c) best fit densities and (d) temperatures of the colder (purple) and warmer (orange) electron components, with the total density and temperature represented by blue lines; (e) best fit kappa values of the warmer electrons; (f) scaled electron density (red) derived from spacecraft potential, compared with those from integration (black) and from best fit (blue) methods.

a channel-half-width higher than Φ_{sc}; the resulting energy gap, from Φ_{sc} to the lower boundary of the lowest preserved channel, is filled (to generate a "new" energy channel) with extrapolations from measurements at adjacent channels. Figure 2b shows the corrected energy spectrum. This extrapolation scheme, linear in energy and logarithmic in phase space density, is based on a reasonable assumption that ambient electron distributions are Maxwellian at low energies. This assumption is supported by the near-logarithmic alignment of data points at the upper three energy channels shown in Figure 2b. The correction also includes the subtraction of Φ_{sc} from the energy of each channel, as the ambient electrons have been accelerated before being recorded.

[18] The corrected spectrum is then integrated to compute the electron density and temperature, shown in Figures 3a and 3b, respectively. Again, the overlapping green lines result from the particle-burst data. The electron density increases from its background level (on the order of 0.01 cm^{-3}, similar to the background proton density) at $\sim$ 1055 UT, and more significantly from 1103 to 1126 UT, when its temperature drops (<20 eV). These two intervals roughly correspond to those in which heavy ions were present.

[19] Before we compare the electron and ion densities directly, however, we note that there are a few sharp jumps in the computed electron density (for example, the back-and-forth jumps at $\sim$ 1104 UT). These jumps indicate a quantization error, probably associated with the relative position of Φ_{sc} to the energy channels. Therefore, an independent method to compute the electron density is required to validate these results.

[20] The new method is to fit the electron distributions to a prescribed function [*Halekas et al.*, 2011], assumed to be a cold Maxwellian superimposed over a warmer kappa distribution [*Vasyliunas*, 1968]. In the best fit procedure, only data from channels with sufficient counts (> 4) are used to avoid statistical error from high-energy electrons with very low count rates, and the photoelectron-contaminated data from channels just above Φ_{sc} are also eliminated. The best fit densities of the colder and the warmer components, as well as their sum, are shown in Figure 3c. The most noteworthy difference between the integrated and the best fit densities is that the sharp jumps in Figure 3a disappear in Figure 3c (the quantization error is eliminated). The otherwise excellent similarities and their similar peak values indicate that both these electron density estimations are most likely accurate.

[21] The best fit electron temperature, as well as the kappa values of the warmer component, are shown in Figures 3d and 3e. By comparing Figure 3d with 3b, however, we find large differences between the best fit and integrated temperatures. These are caused by the removal of high-energy electrons with very low counts in the best fit procedure. These electrons, typically having energies above 1 keV in this event, contribute significantly to temperature. The removal of these high-energy electrons, therefore, results in substantial underestimation of the best fit temperature. The contribution of these electrons to density, on the other hand, is very small (on the order of 10^{-4} cm^{-3}, not shown), which would not affect the aforementioned density similarity between Figures 3a and 3c.

[22] Another way to estimate the electron density is based on current balance between those carried by escaping photoelectrons and by collected ambient electrons [e.g., *Pedersen et al.*, 2008]. The method inputs are the integrated electron temperature (in Figure 3b) and the spacecraft potential Φ_{sc} measured by EFI. The resulting density, scaled with a single factor to match the peak value (at 1112 UT) with those obtained from the other two methods, is shown as the red line in Figure 3f. Despite a difference of about 0.1 cm^{-3} during the 1119–1127 UT interval, the density profile is similar to those from the other two methods (the black and the blue lines in Figure 3f, adopted from Figures 3a and 3c). The similarity confirms that the obtained electron densities (at least before 1119 UT) are reliable, and we can now compare the ion and electron densities to find the best fit mass of the heavy pickup ions.

3.3. Pickup Ion Mass Estimation

[23] The correlation and difference between the uncorrected ion density N_i and the electron density N_e are presented in Figures 4a–4c (as the blue and black lines,

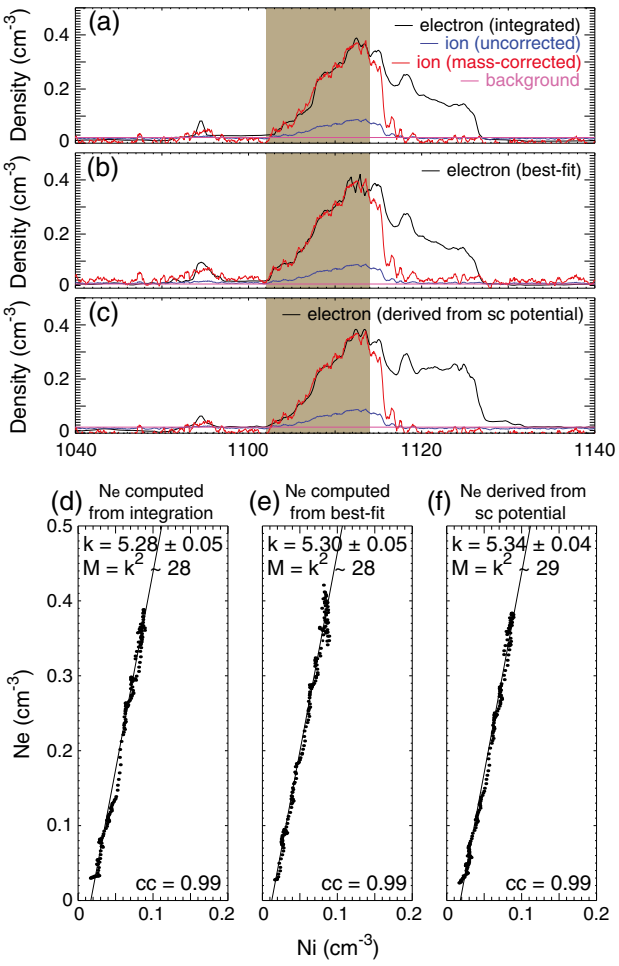

Figure 4. Estimation of the average mass of lunar pickup heavy ions observed on 11 November 2011. (a) Thirty second running averaged ion density N_i (blue) and electron density N_e (black) computed from direct integration. The mass-corrected ion density N_{ic} and the background proton density N_p from linear regression are superimposed as the red and the magenta lines, respectively; (b and c) same as Figure 4a except that N_e are computed from best fit procedures and derived from spacecraft potential measurements, respectively; (d–f) corresponding to Figures 4a–4c, respectively, linear regression results between N_e (derived from three different methods) and N_i.

respectively), by directly comparing the 30 s running averaged ion and electron densities. The N_e values shown in these three panels correspond to the different methods described in section 3.2. The significantly higher values of N_e than N_i clearly indicate the presence of heavy ions between 1102 and 1127 UT, although N_i could be underestimated after 1114 UT when the lowest energy channel started to observed enhanced fluxes implying the possible existence of unrecorded ions at even lower energies (see discussions in section 3.1).

[24] Therefore, the more reliable N_i and N_e values between 1102 and 1114 UT (the shaded interval in Figure 4) are used as inputs to the quasi-neutrality equation,

$$N_e(t) = \sqrt{M} \cdot [N_i(t) - N_p] + N_p, \quad (1)$$

where the background proton density N_p and the heavy ion mass M are two free parameters to be determined via linear regression between N_e and N_i: The best fit M equals the square of the regression line slope k, and the best fit N_p corresponds to the intersection between the regression line and the identity line ($N_e = N_i$).

[25] Using N_e values achieved from the three different methods, we carry out three individual linear regressions. The resultant regression lines, together with data points in the N_i-N_e plane, are displayed in Figures 4d–4f. The corresponding mass-corrected ion densities (N_{ic}, the right-hand side (RHS) of equation (1)) and their proton components N_p are also shown as the red and the magenta lines in Figures 6a–6c, respectively.

[26] Nearly identical results, $M \sim 28$ amu and $N_p \sim 0.02$ cm^{-3}, were achieved from the three linear regressions (which are expected, given the similar N_e values from different methods shown in Figure 3f). The high correlation coefficients of 0.99 suggest excellent match between electron and mass-corrected ion densities within the regression interval from 1102 to 1114 UT. Also, the best fit N_p of $\sim$ 0.02 cm^{-3} approximately agrees with the measured ion and electron densities in the background intervals when heavy ions were absent, even if data from these intervals were not taken into account in the regression procedure.

[27] The most significant mismatch between N_{ic} and N_e appears between 1114 and 1127 UT (outside the regression interval) due to the aforementioned underestimation of N_i after 1114 UT. The other mismatch appears between 1053 and 1056 UT, the relatively short interval when heavy ions were present. The mismatch may correspond to an ion mass much greater than 28 amu (see discussions in *Poppe et al.* [2012] on possible existences of radioactive heavy ions during this interval), although the uncertainty is too large for a definite conclusion (the electron density enhancements obtained from the three methods differ; see Figure 3f).

[28] The otherwise excellent match suggests that the charge quasi-neutrality requirement can indeed be fulfilled, and the estimated average ion mass of 28 amu is consistent with the lower limit of 24 amu derived in *Poppe et al.* [2012]. Our estimations also agree with the *Sarantos et al.* [2012] model, which predicts that Al^+ (M = 27 amu) and Si^+ (M = 28 amu) would be the dominant heavy ion species around the Moon due to their significant production rates in the lunar exosphere, although it is also possible that we observed a mixture of heavier and lighter ions.

[29] We should point out here that the successful application of our technique is largely warranted by the favorable conditions we have in this event. The heavy ions could be easily distinguished from the tenuous lobe population in the ion energy spectra so that we are able to unambiguously identify the background intervals with the absence of heavy ions. Also, the measured proton and electron densities within the background interval agreed with each other, and they were both steady. In the next section, we examine the applicability of this technique to a more complicated event in the plasma sheet where these conditions do not necessarily apply, the event that took place the very next day.

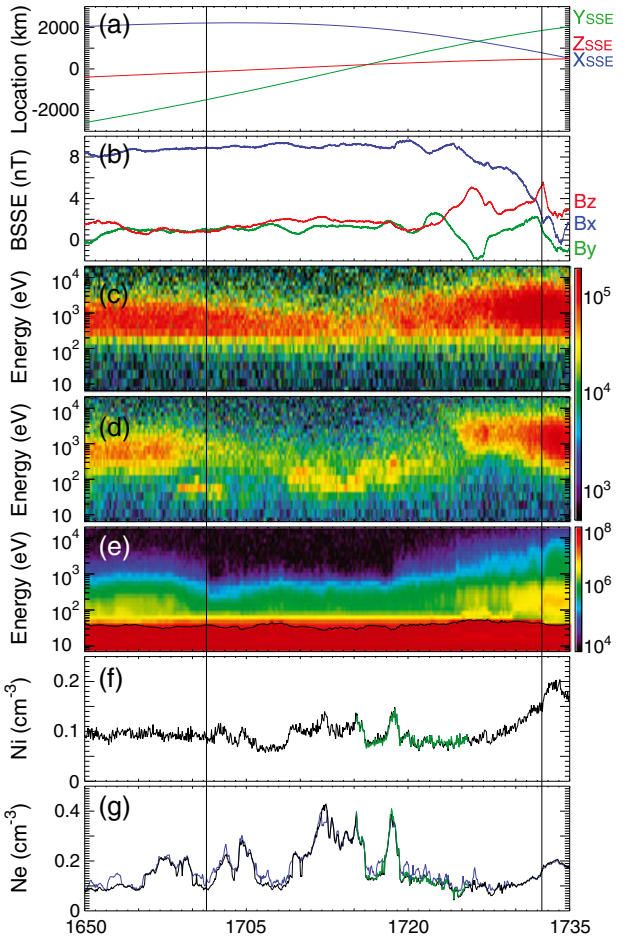

Figure 5. Overview of ARTEMIS P2 observations on 12 November 2011. (a) ARTEMIS P2 location in the SSE coordinates; (b) magnetic field components in SSE; (c and d) ion energy spectra in the moonward and the earthward directions, respectively; (e) electron omnidirectional energy spectra, with the black line representing the spacecraft potential; (f) ion density integrated under the assumption that these ions are protons; and (g) the integrated (black) and the best fit (blue) electron densities. The overlapping green lines in Figures 5f and 5g represent the ion and electron densities integrated from high-resolution particle-burst data, respectively. Again, the two vertical lines bracket the interval when P2 was magnetically connected with the Moon.

4. The 12 November 2011 Event

[30] On 12 November 2011, the Moon remained in the terrestrial magnetotail at GSE [–58.9, –22.0, 0.4] R_E at ~ 1700 UT when ARTEMIS P2 started to move duskward above the dayside lunar surface (P2 position with respect to the Moon is shown in Figure 5a). The magnetic field (in Figure 5b) was dominated by positive B_x most of the time, which suggests that P2 was in the northern plasma sheet (plasma beta ranges from 1.0 to 30 during the 1650–1735 UT interval, not shown). Again, the two vertical lines bracket the interval when P2 was magnetically connected with the lunar surface (under the straight field line approximation, which may be less accurate near the neutral sheet).

[31] Figure 5c is the ion energy spectrum in the moonward direction, in which the background plasma sheet ions (presumably protons) could be seen with substantial fluxes at the 0.1–5 keV energy range. In the earthward direction, the plasma sheet proton fluxes (see Figure 5d) were relatively lower due to the lunar absorption [*Halekas et al.*, 2011; *Harada et al.*, 2012] of earthward moving particles. Superimposed over the plasma sheet population were a series of heavy ion surges in the earthward direction, each lasting a few minutes (comparable with the 3 min gyroperiod of 28 amu ions). These ions appeared at slightly lower but adjacent energies (~ 100 eV), which makes it harder (unlike the previous event) to unambiguously identify the inactive and the active intervals. On the other hand, the electron energy spectrum in Figure 5e shows enhanced fluxes at very low energies just above the spacecraft potential from 1655 to 1725 UT, an electron accumulation signature also shown in the previous event (see Figure 1d) attributable to the plasma quasi-neutrality requirement.

[32] Figure 5f shows the ion density integrated from the measured ion distributions assuming these ions are all protons. The integrated ion density N_i should be accurate, provided that the lowest few energy channels only observed ion fluxes at the noise level indicating that unmeasurable ions at even lower energies were most likely absent. We also use the same methods described in section 3.2 to eliminate photoelectron contaminations and compute the electron density N_e. The resultant N_e from the integration and the best fit methods are shown in Figure 5g as the black and the blue lines, respectively. The N_e and N_i values, despite highly correlated with each other (the peaks and troughs coincide), show very different values from 1655 to 1724 UT, which indicates the underestimation of the real ion density due to the presence of heavy ions.

[33] The correlation between N_e and N_i is also presented in Figure 6a, which shows the 30 s running averaged electron (from integration) and ion densities as the black and the blue lines, respectively. The series of ion surges, indicated by significantly greater N_e values than N_i, all appeared between 1655 and 1724 UT. At other intervals, the N_e and N_i values remain close to each other (despite their variations over time, especially after 1725 UT), indicating the absence of heavy ions. Therefore, we carry out two linear regressions over the active and inactive periods (shown as the two shaded intervals labeled TA and TIA in Figure 6a), and the corresponding regression results (including the data points, the linear regression lines, and the resultant best fit M) are shown in Figures 6d and 6e, respectively. The mass-corrected ion density N_{ic} and the proton component N_p during these intervals are also shown as the red and the magenta lines in Figure 6a.

[34] During the inactive interval from 1725 to 1735 UT, the best fit M equals 1 amu with very small uncertainties (see Figure 6e), which is consistent with the expectations that heavy ions were absent and therefore suggests that the M determination technique is accurate. During the 1655–1724 UT interval in which the series of heavy ion surges appeared, on the other hand, the ion density, even after mass correction, does not always agree with the electron density (see the red and the black lines in Figure 6a) despite a fair correlation coefficient of 0.82. The imperfect match could be caused by N_p (and possibly M) variations during the 1655–1724 UT

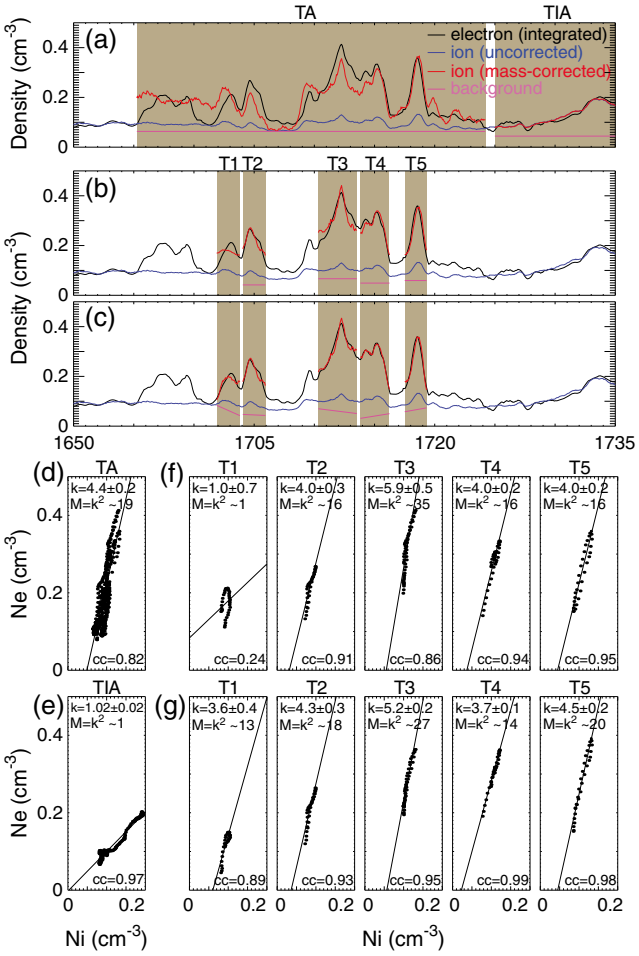

Figure 6. Estimation of the average mass of lunar heavy ions observed on 12 November 2011. (a) Thirty second running averaged electron (black) and ion (blue) densities. The mass-corrected ion density and the background proton density, resulted from linear regressions on both the active and the inactive periods, are superimposed as the red and the magenta lines, respectively; (b) same as Figure 6a except that linear regression is performed in the five shaded intervals, each corresponding to an individual heavy ion surge; (c) same as Figure 6b except that a linear variation of N_p over time is allowed in the regression procedure; (d and e) corresponding to Figure 6a, linear regression results between N_e and N_i during the active and inactive periods, respectively; (f) corresponding to Figure 6b, regression results for the five individual ion surge intervals; and (g) corresponding to Figure 6c, multiple linear regression results between N_e, N_i, and time.

interval; after all, there is no reason that N_p would stay constant in the plasma sheet during the entire interval given the varying densities before and afterward. For example, at 1701 UT, the agreement between N_i and N_e values indicates the absence of heavy ions; the proton density should equal the electron density (0.09 cm^{-3}), nearly 0.03 cm^{-3} higher than the best fit N_p. A more appropriate assumption is that N_p and M both remained constant during each surge of heavy ions (typically within a few minutes). We thus pick five individual ion surges, labeled T1–T5 in Figure 6b, to find the best fit M values during each interval. The linear regression results are shown in Figure 6e. Similarly, the mass-corrected ion density N_{ic} and its proton component N_p are shown as the red and the magenta lines in Figure 6b.

[35] The linear regressions are mostly successful with improved correlation coefficients (shown at the bottom of Figure 6e) except for the T1 interval. The bad correlation at T1, which corresponds to the mismatch between the red and the black lines in Figure 6b and an erroneously large N_p (1.8 cm^{-3}, beyond the figure limit and higher than N_e and N_i), could again be associated with time variations of the proton density during the 2 min interval. By including the first-order gradient term in the $N_p(t)$ expansion around t_0 (the starting moment of the interval), i.e., $N_p(t) = N_{p0} + R(t - t_0)$, equation (1) becomes

$$N_e(t) = \sqrt{M} \cdot N_i(t) + (R - R\sqrt{M}) \cdot (t - t_0) + (1 - \sqrt{M}) \cdot N_{p0}, \quad (2)$$

where R is the N_p change rate within the ion surge interval. The best fit solutions of M, as well as N_{p0} and R, can thus be achieved by multiple linear regressions between N_e, N_i, and time.

[36] Figure 6g shows the correlations between N_i and the t-dependent-term-subtracted N_e with improved correlation coefficients, in which the lines represent the intersections of the regression planes with the $t = t_0$ plane. The mass-corrected ion density (the RHS of equation (2)) is shown in Figure 6c as the red lines, which well agree with the electron density even for the T1 interval. The magenta lines in Figure 6c correspond to the proton density N_p. The N_p variations, consistent with one another despite being obtained from five independent regressions, further justify the validity of the linear $N_p(t)$ variation assumption.

[37] The results suggest that very different ion species, or very different combinations of ion species, were distributed at different locations and/or times above the lunar surface. This explains the observations, for example, that N_e is greater at T2 than at T1 while N_i is higher at T1 (see the black and the blue lines in Figure 6c); they are caused by the heavier ion mass at T2 (18, in the neighborhood of O^+ and OH^+) than at T1 (13, possibly C^+). Also note that the average ion mass is 27 amu at T3, which is very close to the estimated 28 amu in the aforementioned 11 November 2011 event and therefore supports the *Sarantos et al.* [2012] prediction of the Al^+/Si^+ presence in the lunar environment.

[38] The spatial and/or temporal dependence of the lunar heavy ion species, together with their bursty appearances, may be associated with unsteady magnetotail convection (temporally or spatially), the different gyroradii of these ion species, and the species-dependent source regions at the lunar surface (albeit less likely). It is important to analyze this event in greater detail and discuss these possibilities in light of our findings, although these investigations are beyond the scope of this paper and could be addressed in a future study.

[39] It should be also pointed out that the technique fails in analyzing the surge before T1 (between 1650 and 1700 UT when the electron and ion densities disagree, see Figure 6c). The uncorrected ion density N_i was nearly constant during this interval, which would result in a near-vertical regression line and therefore an extremely large M. One possible

explanation is that these ions came from radioactive heavy neutrals (such as ^{222}Rn and its daughter products) vented from localized cracks in the lunar crust [*Lawson et al.*, 2005; *Poppe et al.*, 2012]. Another possibility lies in nonlinear variations of the background proton density; an N_p trough during this interval, together with a peak in the heavy ion density N_h, could compensate each other in the uncorrected ion density ($N_i = N_p + N_h$) as the mass-corrected density ($N_{ic} = N_p + \sqrt{M} \cdot N_h$) peaks.

[40] Finally, we note that our technique is robust against DC offsets in the computations of the ion and electron densities (such as those arising from imperfect background counts removal). Any offsets in N_i or N_e, even if they result in N_i-N_e mismatch during inactive intervals, would only affect the y intercepts of the linear regression line/plane but not the slopes. In other words, while the estimation of the proton density N_p (or N_{p0}) could be vulnerable to DC offsets, the determination of average ion mass M should remain accurate.

5. Summary and Discussion

[41] We presented a new technique based on plasma quasi-neutrality to determine the average mass of lunar pickup ions detected by electrostatic analyzers. The technique was applied to a well-studied event on 11 November 2011, when ARTEMIS/ESA observed pickup ions accompanied by accumulated cold (< 20 eV) electrons to maintain charge quasi-neutrality. After carefully eliminating error sources in the density computations, we showed that the technique resulted in an average ion mass of around 28 amu, which agrees with the lower limit of 24 amu derived in the *Poppe et al.* [2012] model and supports the prediction of Al^+ and Si^+ dominance near the Moon [*Sarantos et al.*, 2012].

[42] We also studied a more complicated event on 12 November 2011 when a series of heavy ion surges were observed by ARTEMIS in the northern plasma sheet above the dayside lunar surface. The technique, after refinements to tolerate uncertain and/or varying background proton densities, was able to achieve the average mass of heavy ions (as well as the proton and heavy ion densities) during each ion surge. The technique resulted in different ion masses between different surges, which suggests a spatial and/or temporal dependence of heavy ion species above the lunar surface (that may deserve a future study).

[43] The model-independent ion mass estimation, besides being compared with the *Poppe et al.* [2012] constraints and the *Sarantos et al.* [2012] predictions as shown in this paper, may also be compared or even combined with particle-tracing inferences [*Halekas et al.*, 2012] to provide model validations and/or further constraints. These efforts, along with the accurate density measurements, will enable usage of highly sensitive ARTEMIS/ESA to study neutrals in the lunar exosphere/surface through pickup ion observations. For example, we plan to statistically analyze the mass of lunar pickup ions in the lobe and compare the results with solar wind counterparts, to examine the relative importance of solar wind surface-sputtering in ion production. Moreover, ARTEMIS will be able to coordinate with the upcoming Lunar Atmosphere and Dust Environment Explorer mission (designed to study the lunar exosphere and dust environment, to be launched this year) at multiple altitudes, to follow lunar constituents before and after ionization and from their source to their escape into space.

[44] **Acknowledgments.** The ARTEMIS mission is operated under NASA contract NAS5-02099. J.S.H. and A.R.P. gratefully acknowledge support from NASA's LASER program, grant NNX13AJ97G. We are also grateful to J. P. McFadden, Y. Nishimura, J. Lewis, J. McTiernan, and P. Cruce for their help with software and to J. Hohl for editorial support.

References

Angelopoulos, V. (2008), The THEMIS mission, *Space Sci. Rev.*, *141*, 5–34.

Angelopoulos, V. (2011), The ARTEMIS mission, *Space Sci. Rev.*, *165*, 3–25., doi:10.1007/s11214-010-9687-2.

Auster, H. U., et al. (2008), The THEMIS fluxgate magnetometer, *Space Sci. Rev.*, *141*, 235–264.

Bonnell, J. W., F. S. Mozer, G. T. Delory, A. J. Hull, R. E. Ergun, C. M. Cully, V. Angelopoulos, and P. R. Harvey (2008), The electric field instrument (EFI) for THEMIS, *Space Sci. Rev.*, *141*, 303–341.

Halekas, J. S., G. T. Delory, W. M. Farrell, V. Angelopoulos, J. P. McFadden, J. W. Bonnell, M. O. Fillingim, and F. Plaschke (2011), First remote measurements of lunar surface charging from ARTEMIS: Evidence for nonmonotonic sheath potentials above the dayside surface, *J. Geophys. Res.*, *116*, A07103, doi:10.1029/2011JA016542.

Halekas, J. S., A. R. Poppe, G. T. Delory, M. Sarantos, W. M. Farrell, V. Angelopoulos, and J. P. McFadden (2012), Lunar pickup ions observed by ARTEMIS: Spatial and temporal distribution and constraints on species and source locations, *J. Geophys. Res.*, *117*, E06006, doi:10.1029/2012JE004107.

Halekas, J. S., A. R. Poppe, G. T. Delory, M. Sarantos, and J. P. McFadden (2013), Using ARTEMIS pickup ion observations to place constraints on the lunar atmosphere, *J. Geophys. Res. Planets*, *118*, 81–88, doi:10.1029/2012JE004292.

Harada, Y., et al. (2012), Nongyrotropic electron velocity distribution functions near the lunar surface, *J. Geophys. Res.*, *117*, A07220, doi:10.1029/2012JA017642.

Hilchenbach, M., D. Hovestadt, B. Klecker, and E. Möbius (1993), Observation of energetic lunar pick-up ions near Earth, *Adv. Space Res.*, *13*, 321–324.

Lawson, S. L., W. C. Feldman, D. J. Lawrence, K. R. Moore, R. C. Elphic, R. D. Belian, and S. Maurice (2005), Recent outgassing from the lunar surface: The lunar prospector alpha particle spectrometer, *J. Geophys. Res.*, *110*, E09009, doi:10.1029/2005JE002433.

Mall, U., E. Kirsch, K. Cierpka, B. Wilken, A. Söding, F. Neubauer, G. Gloeckler, and A. Galvin (1998), Direct observation of lunar pick-up ions near the Moon, *Geophys. Res. Lett.*, *25*, 3799–3802, doi:10.1029/1998GL900003.

McFadden, J. P., C. W. Carlson, D. Larson, V. Angelopoulos, M. Ludlam, R. Abiad, and B. Elliot (2008a), The THEMIS ESA plasma instrument and in-flight calibration, *Space Sci. Rev.*, *141*, 277–302.

McFadden, J. P., C. W. Carlson, D. Larson, J. Bonnell, F. Mozer, V. Angelopoulos, K.-H. Glassmeier, and U. Auster (2008b), THEMIS ESA first science results and performance issues, *Space Sci. Rev.*, *141*, 477–508, doi:10.1007/s11214-008-9433-1.

Nosé, M., K. Takahashi, R. R. Anderson, and H. J. Singer (2011), Oxygen torus in the deep inner magnetosphere and its contribution to recurrent process of O^+-rich ring current formation, *J. Geophys. Res.*, *116*, A10224, doi:10.1029/2011JA016651.

Pedersen, A., et al. (2008), Electron density estimations derived from spacecraft potential measurements on cluster in tenuous plasma regions, *J. Geophys. Res.*, *113*, A07S33, doi:10.1029/2007JA012636.

Poppe, A. R., R. Samad, J. S. Halekas, M. Sarantos, G. T. Delory, W. M. Farrell, V. Angelopoulos, and J. P. McFadden (2012), ARTEMIS observations of lunar pick-up ions in the terrestrial magnetotail lobes, *Geophys. Res. Lett.*, *39*, L17104, doi:10.1029/2012GL052909.

Poppe, A. R., J. S. Halekas, R. Samad, M. Sarantos, and G. T. Delory (2013), Model-based constraints on the lunar exosphere derived from ARTEMIS pickup ion observations in the terrestrial magnetotail, *J. Geophys. Res. Planets*, *118*, 1135–1147, doi:10.1002/jgre.20090.

Sarantos, M., R. E. Hartle, R. M. Killen, Y. Saito, J. A. Slavin, and A. Glocer (2012), Flux estimates of ions from the lunar exosphere, *Geophys. Res. Lett.*, *39*, L13101, doi:10.1029/2012GL052001.

Stern, S. A. (1999), The lunar atmosphere: History, status, current problems, and context, *Rev. Geophys.*, *37*, 453–492, doi:10.1029/1999RG900005.

Tanaka, T., et al. (2009), First in situ observation of the moon-originating ions in the Earth's magnetosphere by map-pace on SELENE (KAGUYA), *Geophys. Res. Lett.*, *36*, L22106, doi:10.1029/2009GL040682.

Vasyliunas, V. M. (1968), A survey of low-energy electrons in the evening sector of the magnetosphere with OGO 1 and OGO 3, *J. Geophys. Res.*, *73*, 2839.

Wang, X.-D., et al. (2011), Detection of m/q = 2 pickup ions in the plasma environment of the Moon: The trace of exospheric H_2^+, *Geophys. Res. Lett.*, *38*, L14204, doi:10.1029/2011GL047488.

Yokota, S., et al. (2009), First direct detection of ions originating from the Moon by map-pace IMA onboard SELENE (KAGUYA), *Geophys. Res. Lett.*, *36*, L11201, doi:10.1029/2009GL038185.